EES Batteries

PAPER

Check for updates

Cu substrate as a bi-directional kinetic promoter for high-efficiency four-electron Sn aqueous batteries

Jianbo Wang, [ID] [a] Sofia K. Catalina, [b] Xin Xu, [ID] †[b,c] Zhelong Jiang, [ID] [b,d] Qin Tracy Zhou, [e] William C. Chueh*[b,c,d] and J. Tyler Mefford*‡[b]

Aqueous batteries utilizing four-electron tin (Sn) anodes are promising candidates for grid-scale energy storage due to their intrinsic safety and high energy density. However, carbon-based anode substrates exhibit non-uniform Sn deposition and sluggish $Sn(OH)_6^{2-}/Sn$ kinetics, limiting voltage efficiency. Here, we employ a copper (Cu) anode substrate that delivers bi-directional kinetic enhancement through Cu–Sn interfacial chemistry. Surface-sensitive analyses unveil an *in situ* formation of a Cu_6Sn_5 alloy interphase during plating and a surface-bound $Sn(OH)_x$ intermediate during oxidation. Benefiting from this strong Cu–Sn affinity, the Cu substrate eliminates the nucleation voltage spike on charge and reduces the second-step discharge overpotential by ~300 mV at 1 mA cm^{-2}, yielding a near-single-plateau voltage profile for this four-electron redox. As a result, the round-trip efficiency of Sn–Ni full cells rises from 70% to 80%, sustained for >200 cycles with improved rate capability. This study underscores the importance of substrate engineering in achieving high efficiency and offers guiding principles for interface-driven optimization in multi-electron aqueous batteries toward practical, long-duration energy storage.

Broader context

Grid-scale energy storage calls for batteries that are safe, low-cost, energy-dense, and highly efficient. Aqueous batteries offer an intrinsically safe and scalable platform, and emerging four-electron tin anodes present a promising opportunity to combine high capacity with long cycle life. However, their voltage efficiency remains limited by sluggish interfacial kinetics. Here we demonstrate that a copper current collector enhances kinetics in both directions, improving voltage efficiency by 10% and sustaining 80% round-trip efficiency over hundreds of cycles without requiring coatings or additives. Operando diagnostics further uncover bi-directional Sn–Cu interfacial interactions, including an overlooked Sn-oxidation electrocatalysis pathway that connects battery interface design with broader electrocatalytic principles. These insights offer a transferable interfacial design strategy for improving performance in aqueous multi-electron systems.

Introduction

The renewable energy transition requires long-duration energy storage technologies with low cost and high safety.[1–4] Aqueous batteries using inexpensive, non-toxic elements and non-flammable electrolytes offer an attractive sustainable solution,[5–7] but their low efficiency and limited cyclability remain significant challenges.[8–10] Recently, Sn has emerged as a promising anode material[11–13] because it can overcome the challenges faced by conventional aqueous metal anodes like Zn.[9,14] The parasitic hydrogen evolution reaction (HER) is less severe on Sn due to its low HER activity[15] and optimal reduction potential near the reversible hydrogen electrode (RHE).[16,17] Sn's more isotropic crystal structure promotes dendrite-free deposition as polyhedral particles.[18,19] Furthermore, up to four electrons can participate in the Sn redox, resulting in a high theoretical capacity of 903 mAh g^{-1} or 6560 Ah L^{-1} for metallic Sn.

Among the four-electron Sn redox options, the alkaline $Sn(OH)_6^{2-}/Sn$ redox couple stands out as the most promising and, to date, the only fully demonstrated chemistry. In 2021, Lu *et al.* developed a Sn–I redox flow battery operating at 60 °C utilizing this redox.[19] Recently, we demonstrated a four-elec-

aDepartment of Chemistry, Stanford University, Stanford, CA 94305, USA
bDepartment of Materials Science & Engineering, Stanford University, Stanford, CA 94305, USA. E-mail: wchueh@stanford.edu, tmefford@ucsb.edu
cStanford Institute for Materials and Energy Sciences, SLAC National Accelerator Laboratory, Menlo Park, CA 94025, USA
dSLAC-Stanford Battery Center, Applied Energy Division, SLAC National Accelerator Laboratory, Menlo Park, CA 94025, USA
eShell International Exploration & Production Inc., Houston, TX 77082, USA
†Present address: The Polytechnic School, Ira. A. Fulton Schools of Engineering, Arizona State University, Mesa, AZ 85212, USA.
‡Present address: Department of Chemical Engineering, University of California, Santa Barbara, Santa Barbara, CA 93106, USA.

tron Sn–Ni static cell at 30 °C and uncovered a kinetically asymmetric redox mechanism involving an intermediate Sn $(OH)_3^-$ species.[20] The $Sn(OH)_3^-$ intermediate impacts cell efficiency in two critical ways: (1) it induces a crossover effect that causes self-discharge and reduces coulombic efficiency (CE), and (2) its sluggish electrochemical oxidation contributes to high overpotential during the second discharge step, lowering voltage efficiency (VE). In prior work, we focused on improving the CE by optimizing the separator to limit Sn $(OH)_3^-$ crossover.[20] However, slow kinetics in the $Sn(OH)_6^{2-}$/Sn $(OH)_3^-$ redox couple remain a bottleneck for VE and rate capability. This VE challenge is further complicated by a substantial nucleation barrier, which introduces significant voltage instability at the onset of charging.

The anode substrate plays a central role in addressing these limitations, as cell voltage is primarily influenced by the electrochemical interface.[21,22] Ideally, the substrate should facilitate efficient plating and stripping, yet this is not the case for graphite used in early studies on four-electron $Sn(OH)_6^{2-}$/Sn redox.[19,20] Other works have shown that Cu-based substrates are well-suited for Sn aqueous anode, enabling uniform plating and low overpotential compared to other common substrates such as C, Fe, Ni and Ti.[23–26] However, these studies mainly focused on the role of substrate in two-electron Sn redox and during the plating direction, with arguments largely based on theoretical calculation that lacks scrutiny at the Cu–Sn interfacial chemistry. Moreover, the kinetically limiting $Sn(OH)_3^-$ oxidation reaction (SnOR) in four-electron discharge remains completely unexplored in the electrocatalysis literature. Motivated by these gaps, we aim to experimentally elucidate how Cu engages with Sn throughout its full four-electron cycle.

In this work, we reveal Cu as a bi-directional catalytic substrate that enhances both Sn deposition kinetics and $Sn(OH)_3^-$ oxidation activity in the $Sn(OH)_6^{2-}$/Sn redox. During charge, the Cu substrate eliminates the voltage peak observed with graphite felt, forming a Cu–Sn alloy interphase as confirmed by X-ray diffraction (XRD) and cross-sectional scanning electron microscopy (SEM). During discharge, the Cu substrate reduces the overpotential of the second discharge step by ~300 mV at 1 mA cm^{-2}. Electrochemical surface-enhanced Raman spectroscopy (EC-SERS) suggests a Cu-bound Sn–OH surface intermediate that contributes to the catalytic effect of Cu on SnOR. Overall, the strong affinity between Cu and Sn promotes rapid kinetics in both directions, leading to nearly single-plateau behavior in both charge and discharge in Sn–Ni full cells. Consequently, the round-trip efficiency (RTE) increases from 70% to 80% with stability maintained over 200 cycles. These results underscore the critical role of substrate in improving battery efficiency, paving the way for more cost-effective, high-performance energy storage solutions.
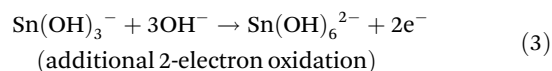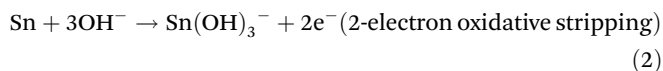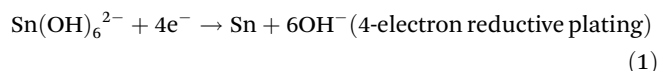
Results and discussion

Improving kinetics in both directions with Cu substrate

Fig. 1a and b compares the morphology of the graphite felt and Cu foam used in this study. Both substrates feature a 3D structure capable of holding the electrolyte within its pores in a pouch cell configuration. Due to the conventional production methods for these materials, the surface area per projected geometric area of Cu foam is over an order of magnitude smaller than that of graphite felt (~7 cm^2 cm$_{geo}^{-2}$ compared to ~124 cm^2 cm$_{geo}^{-2}$ [27,28]). We note that any kinetic benefit from Cu is underestimated under our conditions: at the same geometric current density, the smaller surface area of Cu foam translates to a higher local current density, which—if kinetics were identical—should inherently yield a higher overpotential.

Most studies on substrate effects in plating-stripping reactions in batteries begin with three-electrode flooded cells or two-electrode half cells to evaluate overpotential and efficiency. However, these methods are less representative for the four-electron $Sn(OH)_6^{2-}$/Sn system due to complexity introduced by the $Sn(OH)_3^-$ intermediate and asymmetric kinetics in the two-step mechanism.[20] In contrast, the low-volume Sn–Ni full cell with a cation-exchange membrane (CEM) effectively enables reversible four-electron redox and reveals the asymmetric reaction mechanism through its voltage profile.[20] Therefore, we directly pair the substrates with a $Ni(OH)_2$ cathode in CEM-separated full cells with $Sn(OH)_6^{2-}$ electrolyte to compare their electrochemical behavior within the Sn $(OH)_6^{2-}$/Sn redox system.

The black trace in Fig. 1c shows the voltage profile of the Sn–Ni full cell with a graphite felt anode substrate, as demonstrated in our previous work.[20] The profile features a nucleation peak and single plateau during charge, and two distinct plateaus during discharge more than 300 mV apart from each other, corresponding to the following reactions on the anode:

$$Sn(OH)_6^{2-} + 4e^- \rightarrow Sn + 6OH^- \text{ (4-electron reductive plating)} \tag{1}$$

$$Sn + 3OH^- \rightarrow Sn(OH)_3^- + 2e^- \text{ (2-electron oxidative stripping)} \tag{2}$$

$$Sn(OH)_3^- + 3OH^- \rightarrow Sn(OH)_6^{2-} + 2e^- \\ \text{(additional 2-electron oxidation)} \tag{3}$$

When the graphite substrate is replaced with a Cu foam, the voltage-related issues in both directions were significantly mitigated (red trace in Fig. 1c). During charge, the nucleation peak disappears, indicating significantly improved nucleation kinetics. During discharge, the first plateau appears at a similar potential to that observed with graphite substrate, which is expected since this two-electron stripping step is controlled by the kinetics at the Sn metal–electrolyte interface independent of substrate (eqn (2)). After all Sn is stripped, the second plateau shows a distinctly reduced overpotential by over 300 mV, making it difficult to distinguish the two plateaus, in line with the similar thermodynamic potentials for the two reactions.[16] The results demonstrate that the Cu substrate effectively reduces the nucleation barrier during charge and improves the oxidation of $Sn(OH)_3^-$ during discharge. Fig. 1d compares the VE of cells using the two substrates at 2 mAh cm^{-2} over 200 cycles (800 h). As anticipated from the
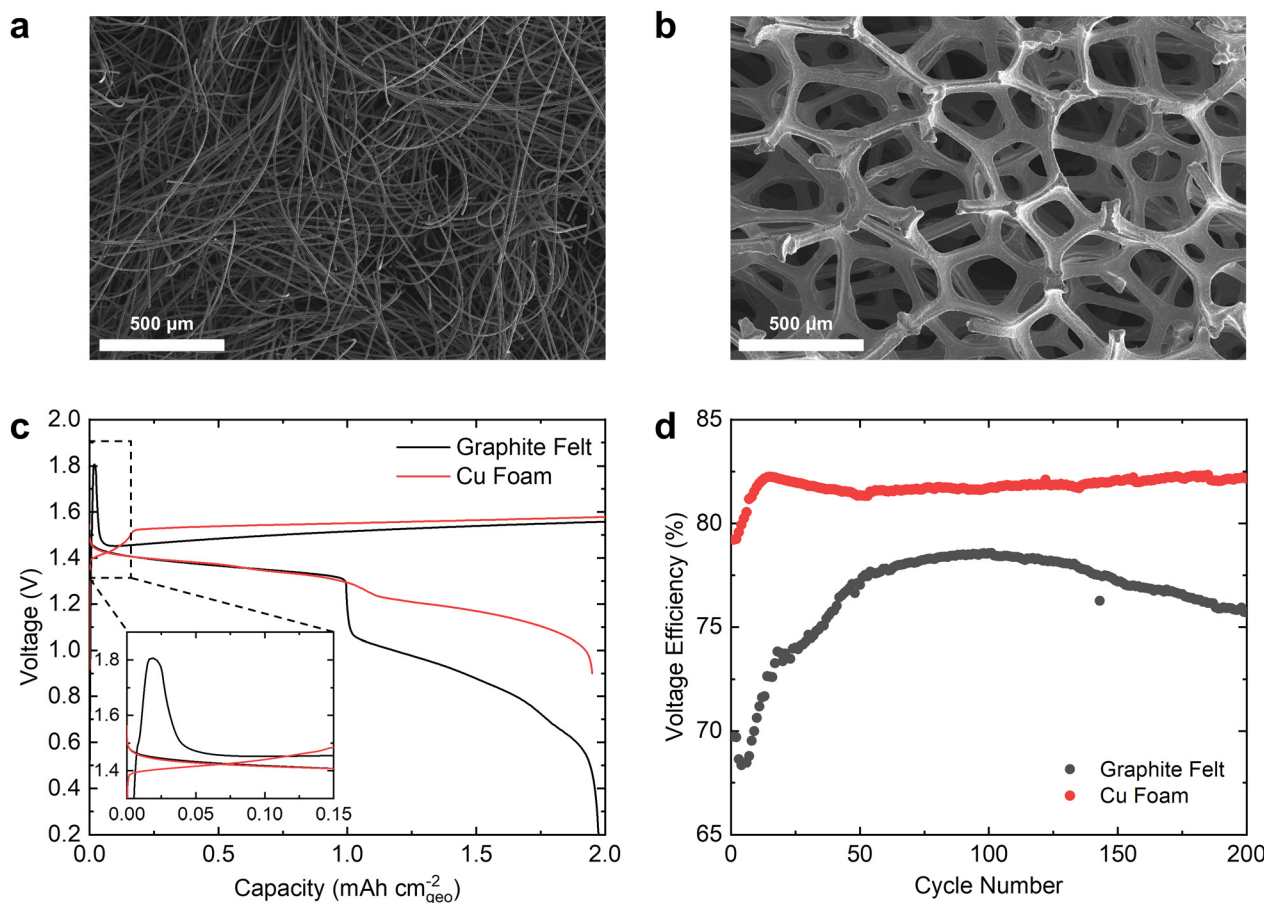
Fig. 1 (a) SEM image of graphite felt. (b) SEM image of Cu foam. (c) Galvanostatic charge–discharge curves of CEM-separated Sn–Ni pouch cells using graphite felt and Cu foam as anode substrates with 1.7 M Sn electrolyte at 1 mA cm^{-2} and 2 mAh cm^{-2} (10th cycle). The cell voltage of Cu substrate cell is limited to above 0.9 V (anode below ~+0.4 V *vs.* RHE) to prevent oxidation of Cu surface during discharge. Inset: comparison of nucleation overpotential at initial plating stage. (d) Comparison of voltage efficiencies between Sn–Ni pouch cells.

enhanced kinetics, the initial VE increases substantially, rising from 71% with the graphite felt to 81% with the Cu foam substrate, with no sign of decay throughout 800 h. The VE improvement further leads to an increase in RTE from 70% to 80% (Fig. S1, SI). In addition, the Cu substrate also enhances rate capability, eliminating the nucleation peak and reducing discharge overpotentials across various current densities (Fig. S2, SI). Note that the enhancement effect of Cu is largely underestimated in this comparison, as the Cu foam surface experiences a significantly higher actual current density due to its much lower surface area (Fig. 1a and b).

To assess whether the mechanism with the graphite substrate demonstrated in the previous work (eqn (1)–(3)) remains consistent on a Cu substrate, we conduct *ex situ* NMR and *operando* XRD measurements on Cu substrate cells. The *ex situ* NMR results for $Sn(OH)_3^-$ and $Sn(OH)_6^{2-}$ progressions (Fig. S3, SI) confirm the formation of $Sn(OH)_3^-$ during discharge. The XRD data reveals that the asymmetric mechanism persists, with a direct plating and a two-step discharge process where Sn is fully stripped during the first step (Fig. S4, SI). Importantly, the cells show an additional peak

(Fig. S4e, SI), which corresponds to an alloy phase Cu_6Sn_5. This peak gradually grows in the initial 4 cycles and will be further discussed in the following section. These results indicate that while the Cu substrate enhances the kinetics of the $Sn(OH)_3^-$ oxidation reaction, it does not transform the two-step discharge mechanism into a single-step, four-electron stripping process. To better understand the improved reaction kinetics, the next sections will investigate the interactions between Cu and Sn during both charging and discharging stages.

Morphology and alloying behavior of Sn deposit on Cu

Fig. 2 compares the plating morphology of Sn particles on the two substrates. On the graphite felt, Sn deposition lacks uniformity on the large scale (Fig. 2a and b) and tends to form discrete particles with minimal contact with the fiber (Fig. 2c). In contrast, Sn deposits more uniformly on Cu (Fig. 2d and e), with finer particles that appears better adhered to the surface (Fig. 2f). The local uniformity is further improved by increasing the plating rate (2 mAh cm^{-2} for 2 h), where Sn deposition shows higher nuclei density and coalesces with each other
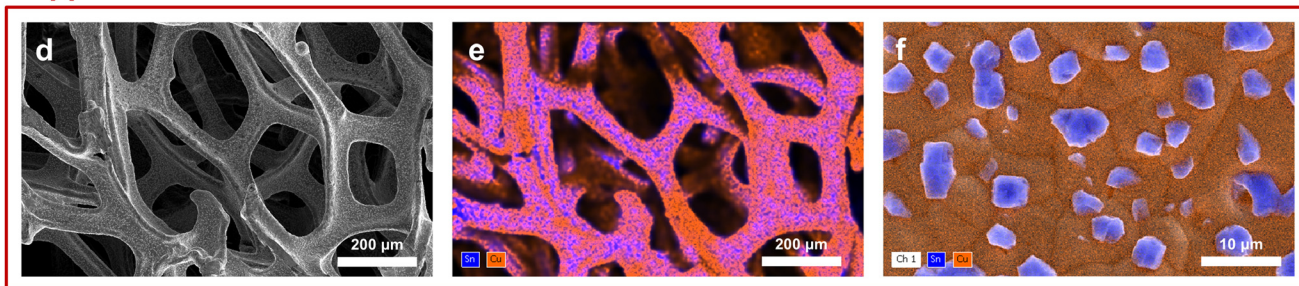
Graphite Felt
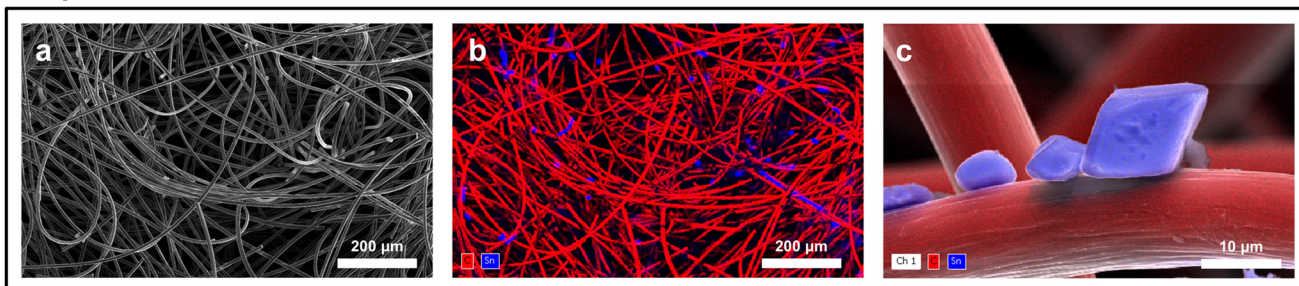
Copper Foam

Fig. 2 SEM characterizations on Sn-deposited substrates after charging at 1 mA cm^{-2} and 2 mAh cm^{-2} in CEM-separated cells with 1.7 M Sn electrolyte. (a–c) Graphite felt substrate. (a) Overview. (b) EDS mapping of (a). (c) Zoom-in EDS mapping. (d–f) Cu foam substrate. (d) Overview. (e) EDS mapping of (d). (e) Zoom-in EDS mapping. EDS mapping are false-colored images where the colors represent elemental distributions: blue for Sn, red for C, and orange for Cu.

(Fig. S5c and d, SI), compared to the discrete particles on the graphite felt (Fig. S5a and b, SI).

Considering the complex geometry and mass transport associated with a Cu foam, we further assess the uniformity of Sn deposition on a Cu foil substrate. As shown in Fig. 3a and c, Sn is plated as a compact, whitish layer consisting of many grains. Notably, after stripping following a few cycles, the surface does not revert to pure copper but is instead covered by a thin, light gray layer of sub-100 nm particles (Fig. 3b and d). The color and morphology are characteristic of Cu$_6$Sn$_5$,[29] a common intermetallic compound (IMC) between Sn and Cu at room temperature, particularly seen in the electrodeposition and solder industries.[30–32] The relative rates of diffusion and reaction promote the growth of "scallop"-shaped IMC into the Sn layer.[30,32]

Fig. 3e displays the cross-sectional SEM image of an individual Sn deposit on a Cu substrate exposed by ion milling. Sn grows on Cu as semi-spherical particles with a broad, uniform contact area, confirming a much better adhesion compared to deposition on graphite felt substrates. A very thin layer (~50 nm) with a distinct contrast is visible between the two phases. Fig. 3f shows the *ex situ* XRD pattern of a Cu particle-based anode (same as *operando* XRD cell) after 20 cycles, further confirming the accumulation of a Cu$_6$Sn$_5$ interphase in 20 cycles. Note that the signal is amplified due to the high surface area of the particle-based anode. In contrast, this peak is negligible in planar or foam electrodes, suggesting that alloy formation is unlikely to consume significant amounts of Sn in practical cells.

In previous works on two-electron Sn aqueous anodes, such an alloy interphase was only inferred from indirect evidence such as peak shifts in X-ray spectra and limited-resolution SEM.[23–25] Here, direct cross-sectional SEM imaging and phase-resolved XRD further corroborate the presence of this interphase.

Overall, the results indicate a significantly stronger affinity for Sn deposition on Cu compared to C-based substrates. Semispherical Sn islands nucleate and grow on the surface, and a Cu$_6$Sn$_5$ IMC is formed in between. During stripping, the IMC partially, if not fully, remains on the surface (Fig. 3d). The subsequent deposition of Sn on the Cu$_6$Sn$_5$ layer is expected to be more adhesive and uniform. This phenomenon might explain the initial shoulder plateau observed at the beginning of later cycles, as shown in Fig. 1c, which returns to the nominal Sn plating potential once the Cu$_6$Sn$_5$ layer is fully covered by Sn. This is in stark contrast to the large barrier required for Sn nucleation on a carbon-based anode in every cycle, where no interphase is formed, and the surface returns to pristine carbon after every stripping.

Catalytic role of Cu in Sn(OH)$_3^-$ oxidation

Next, we investigate the catalytic role of Cu substrates in the Sn (OH)$_3^-$ oxidation reaction (SnOR) during the discharge process. To assess the intrinsic catalytic activity, we use a planar Cu disk electrode in a rotating disk electrode (RDE) setup with a 1 M KOH + 50 mM Sn(OH)$_3^-$ electrolyte. At initial stage, the Cu disk electrode demonstrates minimal activity
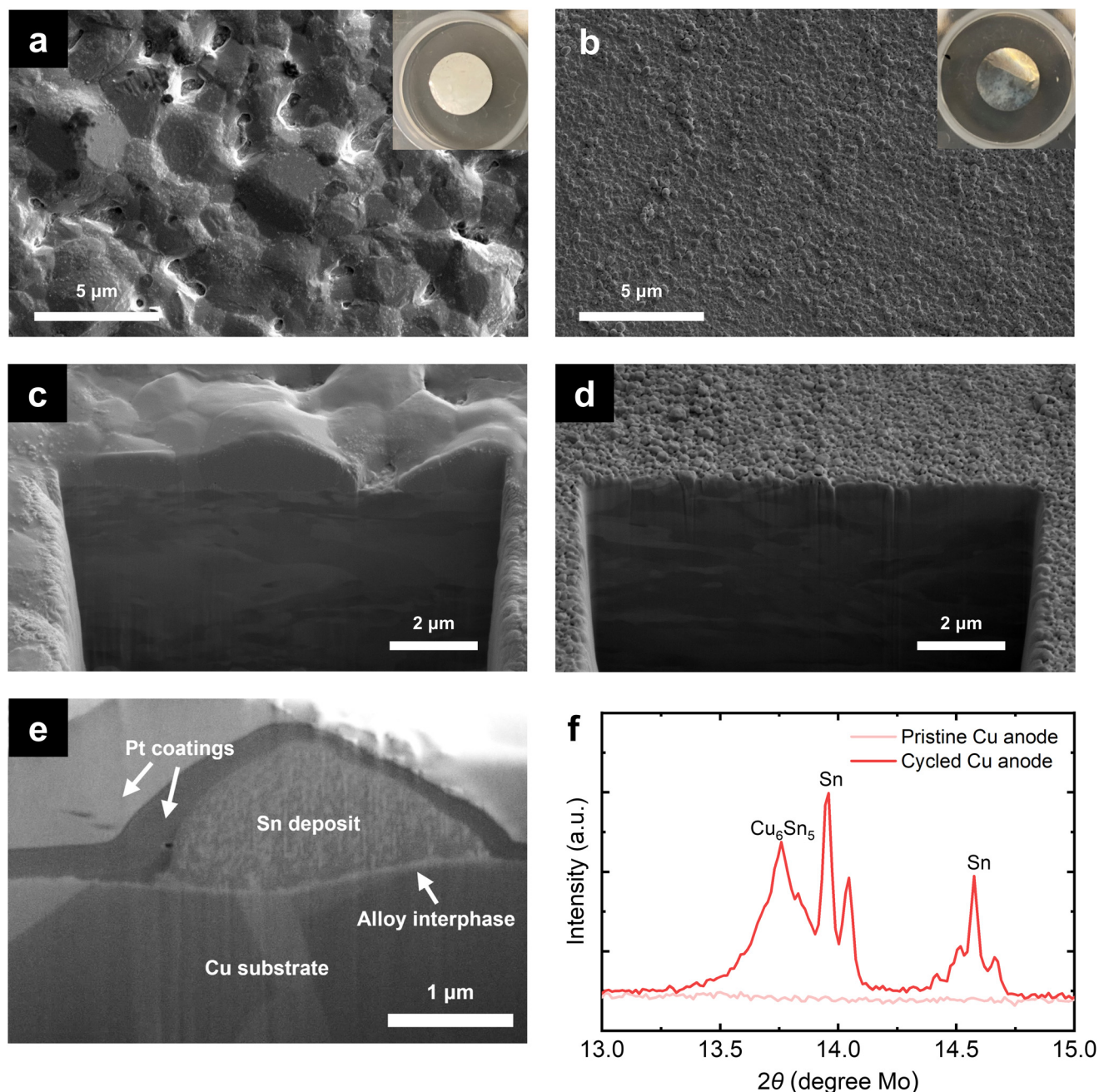
Fig. 3 Characterization of Cu anode substrates after plating and stripping in CEM-separated cells with 1.7 M Sn electrolyte. (a) Top-down SEM image of a Cu foil after charged at 0.25 mA cm^{-2} and 2 mAh cm^{-2}. (b) Top-down SEM image of a Cu foil after 10 cycles at 0.25 mA cm^{-2} and 0.5 mAh cm^{-2}. (c) Cross-sectional view of (a) after ion milling with focused ion beam (FIB). (d) Cross-sectional view of (b) after ion milling with FIB. (e) Cross-sectional SEM image of a Sn-deposited Cu foam after charging at 1 mA cm^{-2} to 8 mAh cm^{-2}. (f) *Ex situ* XRD on a Cu particle-coated electrode before and after cycling at 0.25 mA cm^{-2} and 1 mAh cm^{-2} for 20 cycles.

(Fig. 4a). However, the anodic wave gradually increases under cyclic voltammetry (CV) at 800 rpm rotation, which does not stabilize during the ~3 hour test period, indicating ongoing surface reconstruction that modifies catalytic activity.

This behavior is characteristic of Cu catalysis, where surface-adsorbed intermediates facilitate the mobility of Cu atoms.[33–36] It is thus likely that a similar chemisorption of Sn(OH)$_3^-$ species on Cu occurs during SnOR. Previous studies in

acidic conditions have examined the chemisorption of Sn species on metal electrodes like Au and Pt.[37–39] Among the limited studies available in alkaline media, Sn(OH)$_3^-$ is shown to undergo disproportionation, leading to the growth of a Sn layer on the Cu surface.[40,41] This process, known as autocatalytic deposition, was proposed to proceed *via* a surface hydroxide intermediate. Based on this, we hypothesize that Cu serves an electrocatalyst for SnOR involving a surface *Sn(OH)$_x$ adsor-
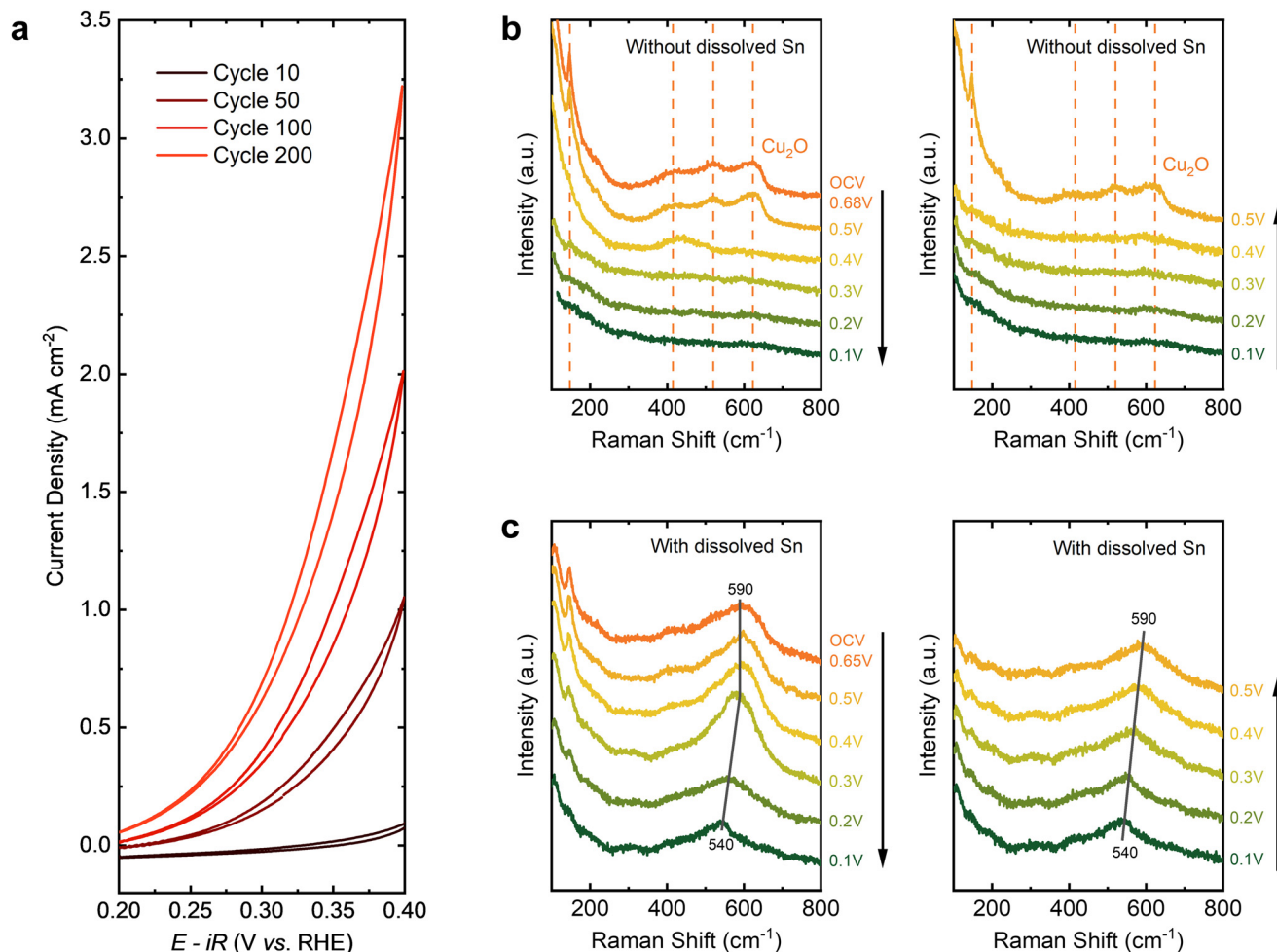
Fig. 4 (a) Cyclic voltammetry on Cu disk in Ar-saturated 1 M KOH + 50 mM Sn(OH)$_3^-$ at 10 mV s^{-1} and 800 rpm. (b) *In situ* EC-Raman spectra on Cu nanoparticle electrode in Ar-saturated 4 M KOH. (Left) Polarization in the cathodic direction from pristine electrode. (Right) Subsequent polarization in the anodic direction. (c) *In situ* EC-Raman spectra on Cu nanoparticle electrode in Ar-saturated 4 M KOH and 0.1 M Sn(OH)$_3^-$ (prepared with 4.1 M KOH and 0.1 M SnO). (Left) Polarization in the cathodic direction from pristine electrode. (Right) Subsequent polarization in the anodic direction. The electrode is scanned and held at each potential (*vs.* RHE) for at least 2 min before taking Raman measurements. Orange dashed lines: Cu$_2$O reference bands.[43,44] Gray solid lines: band assigned to surface Sn(OH)$_x$ (guides to the eye).

bate. In contrast, SnOR on a carbon-based electrode is likely an outer-sphere process with significantly higher kinetic barrier. Although no literature directly addresses SnOR, our proposed mechanism shares several similar aspects to the well-known electrochemical CO oxidation reaction (detailed in note S1, SI).

Due to the instability of the Cu surface during catalysis, it is challenging to infer reaction mechanisms through electrochemical microkinetic analysis. Instead, we utilize electrochemical surface-enhanced Raman spectroscopy (EC-SERS) to detect any adsorbed Sn–OH species on the Cu surface and validate the proposed inner-sphere mechanism on Cu. Previous EC-SERS studies on Cu nanoparticles have successfully detected surface-bound CO intermediates.[42] Here, we adopt a similar approach and compare the EC-SERS spectra on Cu nanoparticles in KOH electrolytes without or with Sn(OH)$_3^-$, respectively (Fig. 4b and c).

The pristine Cu nanoparticles develop a native oxide film upon air exposure, as confirmed by XRD (Fig. S6, SI). This oxide layer is clearly reflected in the Cu$_2$O bands[43,44] in the surface-sensitive Raman spectrum during open-circuit voltage (OCV) before test (Fig. 4b, left). Under cathodic polarization in a Sn-free KOH electrolyte, the oxide feature gradually diminishes around +0.4 V *vs.* RHE, and no signal is observed in the M–O region at lower potentials. During reversed polarization, the Cu$_2$O feature reappears at +0.5 V *vs.* RHE (Fig. 4b, right), consistent with the reduction potential of Cu$_2$O at +0.47 V *vs.* RHE.[16]

In contrast, the spectra on Cu surface with the presence of Sn(OH)$_3^-$ exhibit an additional band peaked at ~590 cm^{-1} (Fig. 4c, left) before any applied bias, which is not observed in control spectra of Cu-KOH system without Sn (Fig. 4b) or bulk Sn(OH)$_3^-$ solution (Fig. S7, SI). This immediate appearance at OCV suggests a pre-equilibrated surface feature of Sn on Cu

instead of formation of new bulk phases. During cathodic polarization, the peak remains around 590 cm^{-1} at potentials above +0.3 V *vs.* RHE before gradually red-shifting to ~540 cm^{-1} at +0.1 V. Under anodic polarization (Fig. 4c, right), the peak shifts back to higher wavenumbers, with no reappearance of Cu$_2$O peaks. Such potential-dependent tuning is a classic signature of a surface-bound species whose bond strength and local field respond to the interfacial potential (vibrational Stark effect). This distinct peak between 540 and 600 cm^{-1} does not correspond to any common peaks within the Cu–O–H system[42,45] and is more likely associated with the additional Sn species. The closest known feature is a surface ν(SnO) mode at 570–580 cm^{-1} observed in various hydrated SnO$_2$, such as hydrothermal SnO$_2$ nanoparticles,[46] precipitated Sn(OH)$_4$[47] or stannic acid β-SnO$_2$·1.3H$_2$O,[48] and Sn oxide sub-nanoclusters with surface OH groups.[49] The observed feature

is thus attributed to a surface-bound Sn-(OH)$_x$ motif, supporting the hypothesized inner-sphere catalytic process. The adsorbed Sn species may also hinder the oxidation of Cu surface by competing with OH$_{ads}$ or O$_{ads}$ on surface sites as in Fig. 4c, right.

The Raman tests shown in Fig. 4b and c were conducted under static conditions with diffusion limitations. To better reflect realistic conditions with sustained catalysis, we perform an additional test with flowing electrolyte (Fig. 5). The Raman signals are collected at the same point without normalization in each overlaid plot to allow a direct comparison of intensity changes. The electrode is further tested at more extreme potentials to evaluate the full redox profile of Sn on Cu.

We first subject the Cu nanoparticle electrode to prolonged cycling and aging, resulting in increased catalytic activity (dashed line, Fig. 5a), consistent with the RDE measurement
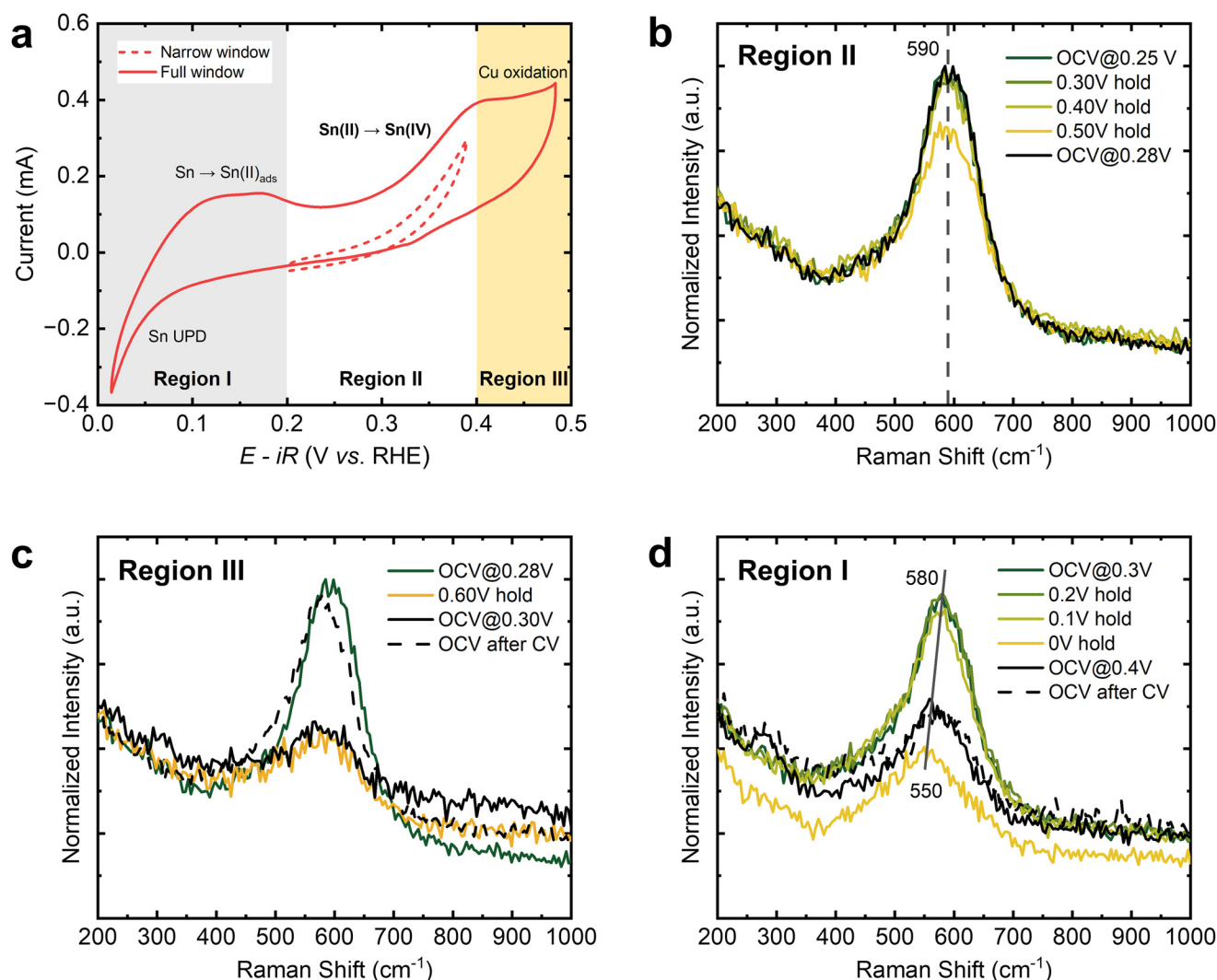
Fig. 5 *In situ* EC-Raman spectra on Cu nanoparticle electrode in Ar-saturated 1 M KOH and 50 mM Sn(OH)$_6$$^{2-}$ with a flow rate of 5 mL min^{-1}. The electrode is scanned and held at each potential (*vs.* RHE) for 1 min before taking Raman measurements. (a) CV at scan rate of 10 mV s^{-1}. Dashed line: scanned between +0.2−0.4 V *vs.* RHE before Raman tests. Solid line: scanned between 0 to +0.5 V *vs.* RHE after Raman tests. (b−d) EC-Raman spectra at series of potentials in corresponding regions in (a). The spectra were taken in the order of the legend labels. "After CV" refer to the spectra of the surface after a CV scan at 10 mV s^{-1} in +0.2 to +0.4 V for 5 cycles and subsequent re-focus.

in Fig. 4a. A CV test over an expanded potential window reveals three distinct regions. Region I (0 to +0.2 V *vs.* RHE) corresponds to the underpotential deposition (UPD) of a monolayer Sn, which occurs at a less negative potential than the bulk plating (overpotential deposition) due to the higher affinity between Sn and Cu than between Sn atoms.[22,50,51] During the anodic scan, Sn is likely oxidized as adsorbed Sn(II). In Region II (+0.2 to +0.4 V *vs.* RHE), the surface and bulk Sn(II) is further oxidized to Sn(IV) before reaching a diffusion limiting current. In Region III above +0.4 V *vs.* RHE, the oxidation of Cu begins to convolute the process.

Fig. 5b–d displays the EC-Raman spectra in these regions. Initial test in Region II (Fig. 5b) shows stable spectra between +0.25–0.4 V, featuring a single peak at 590 cm^{-1} in line with static cell results (Fig. 4c). Upon further anodization to +0.5 V, the peak intensity decreases but fully recovers upon relaxation to OCV, possibly due to a competition between Sn and O species as discussed earlier. Under more anodic polarization at +0.6 V (Fig. 5c), the peak significantly diminishes and is not recoverable at OCV. Nonetheless, the intensity re-emerges after CV scans and refocusing, suggesting surface reconstruction occurring at high potentials. During a negative excursion to Region I (Fig. 5d), the peak persists until reaching 0 V, where it shrinks and shifts to ~550 cm^{-1}, aligning with the static cell spectra in Fig. 4c. The intensity is no longer recoverable even after CV cycles. It can be inferred from Fig. 5a that this sudden irreversible decline comes from Sn UPD. At low potentials, Sn adsorbates naturally release OH$^-$, leading to a reduction in Sn–OH intensity. Additionally, the formation of a thin alloy layer may further attenuate the surface-enhancement effect on Cu irreversibly.[52] Despite the reduced intensity, the peak position shifts back to ~580 cm^{-1} when relaxed to OCV, likely due to a combination of the vibrational Stark[53,54] and UPD effects.[55] Overall, the results in Fig. 5 strongly corroborate the existence of Sn(OH)$_x$ species on Cu surface under dynamic catalytic conditions, which accounts for the superior SnOR activity of the Cu substrate.

Conclusions

This study elucidates the key role of substrate in modulating the reaction kinetics for the four-electron Sn(OH)$_6^{2-}$/Sn redox in the Sn–Ni aqueous batteries, as summarized in Scheme 1. Carbon-based substrates, with their low affinity for Sn, lead to non-uniform Sn deposition during charge and sluggish Sn(OH)$_3^-$ oxidation during discharge (Scheme 1a). In contrast, the Cu substrate significantly improves Sn redox kinetics in both directions due to the strong affinity between Sn and Cu (Scheme 1b). During charge, the Cu substrate promotes the formation of a Cu-Sn alloy (Cu$_6$Sn$_5$) interphase, reducing nucleation barriers and promoting uniform Sn deposition, thereby eliminating voltage spikes observed with C-based substrate. In discharge, Cu catalyzes the SnOR through an inner-sphere mechanism involving a Sn(OH)$_x$ intermediate stabilized by the Cu surface. This intermediate decreases the overpotential required for SnOR. These favorable interfacial dynamics boost VE and RTE by around 10% and significantly enhance rate capability, while preserving the near-unity CE and long cyclability. By bridging atomic-scale mechanistic insights with cell-level performance, this study offers guiding principles for substrate engineering for multi-electron Sn chemistries, advancing the design of more efficient and versatile energy storage systems.

Experimental

Chemicals and materials

Potassium stannate trihydrate (K$_2$SnO$_3$·3H$_2$O, 99.9%), potassium hydroxide (KOH, 99.99%), hydrochloric acid (HCl, 37 wt%), hydrogen peroxide (H$_2$O$_2$, 30 wt%), tin(II) chloride (SnCl$_2$, 98%), tin(II) bromide (SnBr$_2$), deuterium oxide (D$_2$O, 99.9 atom% D), and *N*-methyl-2-pyrrolidone (NMP, 99.5%) were purchased from Sigma-Aldrich. Isopropanol (ACS grade) and Cu powder (APS 10 μm, 99.9% metals basis) were purchased from Fisher Chemical. Sulfuric acid (H$_2$SO$_4$, 10 vol%) and carbon black (Super P, 99+%) were purchased from Alfa Aesar. Cu nanopowders (40 nm, 99.9% metals basis) were purchased from US Research Nanomaterials. Ultrapure water (H$_2$O, 18.2 MΩ resistance) was obtained by purifying deionized water with a Simplicity Water Purification System (Millipore). Argon gas (Ar, 99.999%) was purchased from Praxair. Cu disk (AFED050P040CU) was purchased from Pind Research. Plastic pouches (SealPak 402-24, Kapak, 63.5 μm) were purchased from VWR. Ultra-conductive graphene sheets (25 μm) were purchased from McMaster-Carr. Graphite felt (G280A, AvCarb, 2.8 mm), Vulcan carbon (XC-72R), and Nafion dispersion (5% wt in alcohol) were purchased from Fuel Cell Store. Nafion NR212 membrane (50 μm) was purchased from Ion-Power. Cu foam (MF-Cu16Fom, 99.9%) and polyvinylidene fluoride
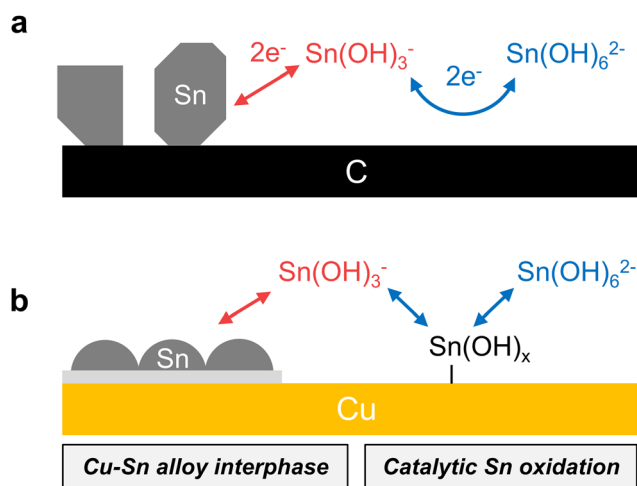
Scheme 1 Schematic representation of the bi-directional promoter effect of Cu in the four-electron Sn(OH)$_6^{2-}$/Sn redox system. (a) On a C-based substrate. (b) On a Cu-based substrate.

(EQ-Lib-PVDF, ≥99.5%) were purchased from MTI Corporation.

Assembly and testing of Sn–Ni pouch cells

Nafion NR212 sheets were cut into squares with protective layers peeled off. The membranes were sequentially treated with 3% H_2O_2 at 80 °C for 1 h, 5% H_2SO_4 at 80 °C for 1 h, and 1 M KOH at 80 °C for 2 h. After each treatment step, the membranes were cooled down and washed copiously with water. Finally, the membranes were dried at 60 °C overnight and stored at room temperature. Eneloop rechargeable Ni-MH AA batteries (BK-3MCCA16FA, Panasonic) were discharged at 50 mA to 1.2 V, and the cathode rolls were harvested and cut into squares.

Graphene sheets were cut into pairs of strips as tabs and sealed at 160 °C between two pieces of pouch layers with a hot melt adhesive (MTI). A cathode (1.4×1.4 cm^2), a separator (2.1×2.1 cm^2), and an anode substrate (graphite felt or Cu foam, 1 cm^2 disk) were placed in order between the two tabs in the pouch. Three sides were sealed at 140 °C leaving one side for electrolyte injection. The 1.7 M Sn electrolyte was prepared by dissolving 100 mmol (5.61 g) KOH and 200 mmol (59.8 g) $K_2SnO_3 \cdot 3H_2O$ in 100 g H_2O, resulting in 0.86 M KOH and 1.7 M $K_2Sn(OH)_6$ (density: 1.42 g mL^{-1}). The electrolyte was injected into the pouch with a micropipette, with 200 μL between anode and separator and 30 μL between cathode and separator. The final side was sealed in a vacuum sealer (MSK-115-III, MTI) at 140 °C. For all four sides, the edges of the separators were sealed between the pouches to avoid electrolyte leakage across the gaps, especially in the cases of ion-selective membranes. No external pressure was applied during electrochemical testing.

For galvanostatic charge–discharge tests, the pouch cells were placed in a temperature chamber (IC-150R, IncuMax) at 30 °C and connected to an external battery cycler (BCS-805, BioLogic). Constant current density of 1 mA cm$_{anode}^{-2}$ was applied based on the projected geometric area of the anode substrate. The cells were charged to 2 mAh cm$_{anode}^{-2}$ and discharged to a cut-off voltage of 0.2 V for graphite felt substrate, or 0.9 V for Cu foam substrate to prevent Cu oxidation.

Scanning electron microscopy

Regular SEM characterization was conducted using an Apreo S LoVac Scanning Electron Microscope (Thermo Fisher Scientific) with an acceleration voltage of 5.0 kV and beam current of 50 pA at a working distance of 10 mm, in standard mode using an Everhart–Thornley detector for secondary electrons. For EDS analysis, the SEM was operated at 20 kV with a Bruker XFlash 6-60 SDD detector.

Cross-sectional SEM images were obtained using a FEI Helios NanoLab 600i FIB/SEM system. For Fig. 3e, a protective layer of platinum (Pt) was first deposited onto the sample electrodes using an electron beam (5 kV, 1.4 nA) to achieve a thickness of approximately 200 nm. This was followed by a ~1.5 μm thick Pt layer deposited via ion beam (Ga$^+$, 30 kV, 80 pA). Subsequent bulk material removal was performed using a Ga$^+$ ion beam at 30 kV and 2.5 nA. The exposed cross-sectional surface was then cleaned with successive ion beam steps at 30 kV, first with 0.79 nA and then with 40 pA. Cross-sectional images were captured at a tilt angle of 52° using the Elstar in-lens secondary electron detector.

X-ray diffraction

Ex situ XRD was performed in the transmission geometry using a Panalytical Empyrean diffractometer with Mo Kα X-ray source ($\lambda_{K\alpha_1}$ = 0.7093 Å, $\lambda_{K\alpha_2}$ = 0.7136 Å). The incident beam from the line-focus X-ray tube was focused using focusing mirror optics, and the diffracted beam was detected using GaliPIX^{3D} detector in scanning line detector mode. The measurements were done either with spinning capillaries (for powder sample in Fig. S6), or with intact electrodes sealed in an empty pouch (Fig. 3f). For spinning capillary measurement of the scrapped material, the sample was compacted inside a "special glass" capillary (Charles Supper). For measurement of the intact electrode, the electrode is fixed at the goniometer center, with the incident X-ray beam being normal to the electrode surface. During the measurement, the X-ray tube remained fixed and only the detector moved along the goniometer circle.

Thin pouch cells for *operando* XRD were constructed as follows. $Ni(OH)_2$ cathode powder was collected by sonicating a piece of Eneloop cathode in water and removing the Ni foam current collector. The suspension was washed with water to neutral pH, and the powder was collected by centrifugation at 6000 rpm and dried at 60 °C overnight. The cathode slurry was prepared by mixing the cathode powder, Super P carbon and PVDF in a 90 : 5 : 5 weight ratio together with NMP. The anode slurry was prepared by mixing 475 mg Cu powder and 25 mg PVDF in 0.35 mL NMP. Electrodes were prepared by coating the slurry onto a graphene sheet using a doctor blade with a 80 μm (anode) or 250 μm (cathode) nominal thickness, and were subsequently dried in a vacuum oven at 60 °C overnight. The mass loadings of the Cu powder and the cathode powder are 3 and 5 mg cm^{-2}, respectively. The pouch cells were assembled using a 1 cm^2 anode, a 2 cm^2 cathode, a CEM separator, and 50 μL of 1.7 M Sn electrolyte on each side. Excess electrolyte was gently squeezed out before vacuum-sealing the final side to minimize the cell thickness.

Operando XRD was performed with Panalytical Empyrean diffractometer using Mo Kα X-ray source tube ($\lambda_{K\alpha_1}$ = 0.7093 Å, $\lambda_{K\alpha_2}$ = 0.7136 Å). The pouch cells were pressurized between two thin beryllium plates using a vertical holder and placed in the diffractometer. Galvanostatic charge–discharge tests were performed with a BioLogic SP-300 potentiostat at 0.25 mA cm$_{anode}^{-2}$ at room temperature. The cells were charged to 0.5 mAh cm$_{anode}^{-2}$ and discharged to 0.9 V (Cu-based anode). Using focusing mirror optics, the X-ray beam was shone through the pouch cell with normal incidence to the electrodes. The diffracted beam was detected using GaliPIX^{3D} detector in static line detector mode between 2θ = 11.5–18.5°, and each scan was collected over a 60 s acquisition time initiated every 90 s.

^{119}Sn nuclear magnetic resonance

Pouch cells were assembled with Cu foam substrates (2×2 cm^2), Ni(OH)$_2$ cathodes (2×2 cm^2), CEM separators (3×3 cm^2), and 1.7 M Sn electrolyte (800 μL anolyte, 60 μL catholyte). After OCV rests for 14 h, galvanostatic tests were conducted at 2 mA cm$_{anode}^{-2}$ and 4 mAh cm$_{anode}^{-2}$ at 30 °C and were stopped at different stages in the first cycle (Fig. S3a). The cells were transferred to an Ar-filled glovebox, where 400 μL anolyte was extracted and transferred to an NMR tube. For calibration curves, a series of samples containing different concentrations of Sn(OH)$_6^{2-}$ or Sn(OH)$_3^{-}$ were prepared by dissolving K$_2$SnO$_3$·3H$_2$O or SnBr$_2$ in 1 M KOH solution. 50 μL D$_2$O was added to each tube, and a thin coaxial tube containing 500 μL of 34 m SnCl$_2$ in concentrated HCl (15 g in 5 mL HCl) was inserted. NMR measurements were performed using a Bruker Neo 400 MHz NMR spectrometer. The solvent is set to 90% H$_2$O 10% D$_2$O (H$_2$O + D$_2$O) and auto-shimming and tuning were used. 300 scans (30 min) were collected for each sample. MestReNova software was used to perform an auto phase correction and 3rd order Bernstein Polynomial fit baseline correction. Concentrations were evaluated using calibration curves based on the peak area ratios between the tested Sn species and the SnCl$_2$ reference.

Cyclic voltammetry

CV test was conducted in an alkaline-resistant PTFE cell (AF01CKT1001, Pine Research) using a VSP-300 potentiostat (BioLogic). A Cu disk insert was inserted into an RRDE electrode with Pt ring (E6R1, Pine Research). The RRDE was polished with Al$_2$O$_3$ suspension (Allied High Tech Products, particle size 0.05 μm) to a mirror finish, and the polishing media was sonicated off in a mixture of isopropanol and water (1 : 1 v/v) followed by copious washing with ultrapure water. Ar was bubbled through the electrolyte for at least 20 min and was kept purging throughout the test. The electrode was immersed in the electrolyte, together with a leakless Ag/AgCl reference electrode (ET069, eDAQ) and a coiled Pt wire counter electrode (99.95%, Thermo Fisher Scientific). The voltage of the Ag/AgCl reference was standardized against a bulk RHE electrode (Hydroflex Hydrogen Reference Electrode, eDAQ). The CV and RDE measurements were conducted at a scan rate of 10 mV s^{-1} and rotation rate of 800 rpm (MSR Rotator, Pine Research).

Electrochemical surface-enhanced Raman spectroscopy

EC-SERS was conducted in a Raman electrochemical flow cell with a leakless Ag/AgCl reference electrode and a Pt wire counter electrode. For the working electrode, 50 mg of Cu nanopowder was dispersed in 1.25 mL of isopropanol with 7.5 μL of Nafion solution. After sonication for 15 min, 50 μL of the dispersion was dropped cast on a glassy carbon square (1 × 1 cm^2, Sigradur) and dried in air. After assembly, the Raman cell was transferred to an Ar-filled glovebox, where the test electrolyte was flowed through to fill the chamber. The cell was then sealed on both ends and transferred to the Raman facil-

ity. The electrochemistry was controlled by a SP-300 portable potentiostat (BioLogic). The potential was scanned to each desired potential at 10 mV s^{-1} and held for at least 1 min before the Raman spectra were recorded.

Results in Fig. 4 were recorded on a Horiba LabRAM HR Evolution Confocal Raman Microscope with an excitation wavelength of 638 nm, and Fig. 5 was recorded on a Horiba Xplora + Confocal Raman Optical Microscope with a 633 nm excitation laser. In either case, the spectrometer was calibrated with a Si wafer. The measurements were conducted using a 100× LWD (long working distance) Olympus objective, a monochromator with a 600 grooves per mm grating, and a 10% neutral density filter. Each spectrum presented is an average of four acquisitions, each with a duration of 30 seconds. For the tests in Fig. 5, the Raman cell was modified to ensure maximum flow through the space above the working electrode. A syringe pump was connected to the cell to deliver the electrolyte at a flow rate of 5 mL min^{-1}.

Author contributions

J. T. M., W. C. C. and Q. T. Z. supervised the project. J. T. M. and J. W. conceived the idea. J. W. designed the experiments and performed CV and EC-SERS measurements. J. W. and S. K. C. developed the pouch cell assembly and performed cell testing. S. K. C. performed the NMR measurements. J. W. and X. X. performed the SEM characterizations. J. W. and Z. J. performed the XRD measurements. All authors contributed to discussion of the results and writing of the manuscript.

Conflicts of interest

J. T. M. has filed a patent application (US17/762016) related to this invention.

Data availability

All data supporting the findings of this study are available within the article and its supplementary information (SI). Supplementary information is available. See DOI: https://doi.org/10.1039/d5eb00176e.

Acknowledgements

References

1 S. Chu and A. Majumdar, *Nature*, 2012, **488**, 294–303.

2 S. Chu, Y. Cui and N. Liu, *Nat. Mater.*, 2017, **16**, 16–22.

3 J. B. Goodenough, *Energy Environ. Sci.*, 2013, **7**, 14–18.

4 Z. Zhu, T. Jiang, M. Ali, Y. Meng, Y. Jin, Y. Cui and W. Chen, *Chem. Rev.*, 2022, **122**, 16610–16751.

5 D. Chao, W. Zhou, F. Xie, C. Ye, H. Li, M. Jaroniec and S.-Z. Qiao, *Sci. Adv.*, 2020, **6**, eaba4098.

6 Y. Liang and Y. Yao, *Nat. Rev. Mater.*, 2023, **8**, 109–122.

7 X. Ji, *Energy Environ. Sci.*, 2019, **12**, 3203–3224.

8 J. Shin and J. W. Choi, *Adv. Energy Mater.*, 2020, **10**, 2001386.

9 D. Stock, S. Dongmo, J. Janek and D. Schröder, *ACS Energy Lett.*, 2019, **4**, 1287–1300.

10 G. Zampardi and F. L. Mantia, *Nat. Commun.*, 2022, **13**, 687.

11 W. Zhou, S. Ding, D. Zhao and D. Chao, *Joule*, 2023, **7**, 1104–1107.

12 H. Zhang, D. Liu, K. Xu and Y. S. Meng, *Adv. Mater.*, 2025, e2417757.

13 X. Lan, Z. Zhang, G. Liao, W. Du, Y. Zhang, M. Ye, Z. Wen, Y. Tang, X. Liu and C. C. Li, *ACS Appl. Mater. Interfaces*, 2025, **17**, 24763–24777.

14 C. Li, S. Jin, L. A. Archer and L. F. Nazar, *Joule*, 2022, **6**, 1733–1738.

15 S. Trasatti, *J. Electroanal. Chem. Interfacial Electrochem.*, 1972, **39**, 163–184.

16 M. Pourbaix, *Atlas of Electrochemical Equilibria in Aqueous Solutions*, National Association of Corrosion Engineers, Houston, 2nd edn, 1974.

17 F. Séby, M. Potin-Gautier, E. Giffaut and O. F. X. Donard, *Geochim. Cosmochim. Acta*, 2001, **65**, 3041–3053.

18 M. J. Mehl, D. Hicks, C. Toher, O. Levy, R. M. Hanson, G. Hart and S. Curtarolo, *Comput. Mater. Sci.*, 2017, **136**, S1–S828.

19 Y. Yao, Z. Wang, Z. Li and Y. Lu, *Adv. Mater.*, 2021, **33**, 2008095.

20 J. Wang, S. K. Catalina, Z. Jiang, X. Xu, Q. T. Zhou, W. C. Chueh and J. T. Mefford, *Joule*, 2024, **8**, 3386–3396.

21 R. A. Huggins, *Advanced Batteries: Materials Science Aspects*, Springer, 2009.

22 N. Eliaz and E. Gileadi, *Physical Electrochemistry: Fundamentals, Techniques, and Applications*, Wiley, 2019.

23 W. Zhou, M. Song, P. Liang, X. Li, X. Liu, H. Li, T. Zhang, B. Wang, R. Zhao, Z. Zhao, W. Li, D. Zhao and D. Chao, *J. Am. Chem. Soc.*, 2023, **145**, 10880–10889.

24 H. Zhang, D. Xu, F. Yang, J. Xie, Q. Liu, D.-J. Liu, M. Zhang, X. Lu and Y. S. Meng, *Joule*, 2023, **7**, 971–985.

25 D. Xu, J. Xie, L. Zhou, F. Yang, Y. Wang, Z. Yang, F. Wang, H. Zhang and X. Lu, *Small*, 2023, e2301931.

26 S. Zhu, Y. Liu and H. Chen, *ACS Appl. Energy Mater.*, 2025, **8**, 4176–4183.

27 J. Y. Kim, G. Liu, M. X. Tran, R. E. A. Ardhi, H. Kim and J. K. Lee, *J. Mater. Chem. A*, 2019, **7**, 12882–12892.

28 A. Mukhopadhyay, Y. Yang, Y. Li, Y. Chen, H. Li, A. Natan, Y. Liu, D. Cao and H. Zhu, *Adv. Funct. Mater.*, 2019, **29**, 1903192.

29 Z. Ni, D. Yang, Y. Wang, W. Yang, B. Deng, J. Hou, Y. Zhang, X. Li and Y. Zhang, *J. Alloys Compd.*, 2022, **906**, 164307.

30 K. Chen, D. Wang, H. Ling, A. Hu, M. Li, W. Zhang and L. Cao, *J. Mater. Sci.: Mater. Electron.*, 2018, **29**, 19484–19490.

31 M. Sobiech, C. Krüger, U. Welzel, J.-Y. Wang, E. J. Mittemeijer and W. Hügel, *J. Mater. Res.*, 2011, **26**, 1482–1493.

32 H. K. Kannojia and P. Dixit, *J. Mater. Sci.: Mater. Electron.*, 2021, **32**, 6742–6777.

33 R. Amirbeigiarab, J. Tian, A. Herzog, C. Qiu, A. Bergmann, B. R. Cuenya and O. M. Magnussen, *Nat. Catal.*, 2023, **6**, 837–846.

34 S. H. Lee, J. C. Lin, M. Farmand, A. T. Landers, J. T. Feaster, J. E. A. Acosta, J. W. Beeman, Y. Ye, J. Yano, A. Mehta, R. C. Davis, T. F. Jaramillo, C. Hahn and W. S. Drisdell, *J. Am. Chem. Soc.*, 2021, **143**, 588–592.

35 A. Auer, M. Andersen, E.-M. Wernig, N. G. Hörmann, N. Buller, K. Reuter and J. Kunze-Liebhäuser, *Nat. Catal.*, 2020, **3**, 797–803.

36 M. Li, M. T. Curnan, W. A. Saidi and J. C. Yang, *Nano Lett.*, 2022, **22**, 1075–1082.

37 D. Mandler and A. J. Bard, *J. Electroanal. Chem. Interfacial Electrochem.*, 1991, **307**, 217–228.

38 E. Lamy-Pitara, L. E. Ouazzani-Benhima, J. Barbier, M. Cahoreau and J. Caisso, *J. Electroanal. Chem.*, 1994, **372**, 233–242.

39 V. A. Vicente and S. Bruckenstein, *Anal. Chem.*, 1972, **44**, 297–300.

40 A. Molenaar and J. J. C. Coumans, *Surf Technol*, 1982, **16**, 265–275.

41 A. Molenaar and J. W. G. de Bakker, *J. Electrochem. Soc.*, 1989, **136**, 378–382.

42 Y. Zhao, X. Chang, A. S. Malkani, X. Yang, L. Thompson, F. Jiao and B. Xu, *J. Am. Chem. Soc.*, 2020, **142**, 9735–9743.

43 A. Singhal, M. R. Pai, R. Rao, K. T. Pillai, I. Lieberwirth and A. K. Tyagi, *Eur. J. Inorg. Chem.*, 2013, 2640–2651.

44 N. Bodappa, M. Su, Y. Zhao, J.-B. Le, W.-M. Yang, P. Radjenovic, J.-C. Dong, J. Cheng, Z.-Q. Tian and J.-F. Li, *J. Am. Chem. Soc.*, 2019, **141**, 12192–12196.

45 I. V. Chernyshova, P. Somasundaran and S. Ponnurangam, *Proc. Natl. Acad. Sci. U. S. A.*, 2018, **115**, E9261–E9270.

46 J. Zuo, C. Xu, X. Liu, C. Wang, C. Wang, Y. Hu and Y. Qian, *J. Appl. Phys.*, 1994, **75**, 1835–1836.

47 B. X. Huang, P. Tornatore and Y.-S. Li, *Electrochim. Acta*, 2001, **46**, 671–679.

48 A. I. Karelin, L. S. Leonova, N. S. Tkacheva, S. E. Nadkhina and Y. A. Dobrovolsky, *Heliyon*, 2022, **8**, e11450.

49 A. Kuzume, M. Ozawa, Y. Tang, Y. Yamada, N. Haruta and K. Yamamoto, *Sci. Adv.*, 2019, **5**, eaax6455.

50 J. Horkans, I. H. Chang, P. C. Andricacos and H. Deligianni, *J. Electrochem. Soc.*, 1995, **142**, 2244–2249.

51 L. A. Azpeitia, C. A. Gervasi and A. E. Bolzán, *Electrochim. Acta*, 2019, **298**, 400–412.

52 J. C. Ingram and J. E. Pemberton, *Langmuir*, 1992, **8**, 2040–2048.

53 S. Zou and M. J. Weaver, *J. Phys. Chem.*, 1996, **100**, 4237–4242.

54 D. K. Lambert, *Electrochim. Acta*, 1996, **41**, 623–630.

55 S. Kania and R. Holze, *Surf. Sci.*, 1998, **408**, 252–259.